ACS OMEGA

http://pubs.acs.org/journal/acsodf

Article

Improved Stable Drag Reduction of Controllable Laser-Patterned Superwetting Surfaces Containing Bioinspired Micro/Nanostructured Arrays

Wanting Rong, Haifeng Zhang, Zhigang Mao, Liang Chen,* and Xiaowei Liu*

Cite This: *ACS Omega* 2022, 7, 2049−2063

Read Online

ACCESS | Metrics & More | Article Recommendations | Supporting Information

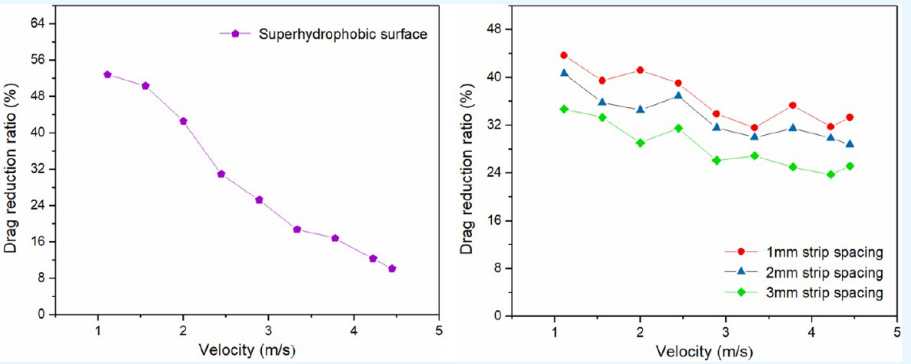

ABSTRACT: Superwetting surfaces are widely used in many engineering fields for reducing energy and resistance loss. A facile and efficient method using laser etching has been used to fabricate and control superwettable drag reduction surfaces. Inspired by the self-cleaning theory of lotus leaves, we propose controllable patterned bionic superhydrophobic surfaces (BSSs) simulating the uneven micro/nanostructures of lotus leaves. The superhydrophobicity and drag reduction ratios at low velocities are highly improved using a laser ablation method on metal substrates. However, unstable air layers trapped on superhydrophobic surfaces are usually cut away by a high-velocity flow, which greatly reduces the drag reduction performance. The fabricated bionic superhydrophobic/hydrophilic surfaces (BSHSs) with alternated hydrophilic strips can build a large surface energy barrier to bind the three-phase contact line. It maintains the stable drag reduction by capturing the air bubbles attached to the hydrophilic strips at a high velocity. Three-dimensional simulation analysis and equipment to measure the weak friction of a self-assembled solid−liquid interface are used to explain the drag reduction mechanism and measure the drag reduction ratios at different flow speeds. BSSs achieve an improved drag reduction effect (maximum 52.76%) at a low velocity (maximum 1.5568 m/s). BSHSs maintain an improved and steady drag reduction effect at high speed. The drag reduction ratios can be maintained at about 30% at high speed, with a maximum value of 4.448 m/s. This research has broad application prospects in energy saving, liquid directional transportation, and shipping due to their robust superhydrophobic properties and stable drag reduction effect.

INTRODUCTION

Energy conservation and pollution reduction have had significant implications in scientific research and engineering in the past. From 1950 to 2001, fuel consumption of the shipping industry has increased from 65 to 280 million tons. The surface friction of the ship consumes more than half of the energy in ocean exploitation and shipping engineering. Shipping accounts for 10% of global carbon transport emissions.[1,2] The United States has built more than two million kilometers of pipelines to carry oil and natural gas.[3] Pipe wall friction drag during liquid transportation can greatly reduce the efficiency of transportation. Constructing biomimetic shark-shaped micro/nanostructures on the surfaces of aircraft can reduce surface drag by 8% and reduce energy consumption by 1.5%.[4,5] Engineering efficiency, energy conservation, and emission reduction can be improved by drag reduction.[6−9] Therefore, achieving efficient drag reduction in many fields, such as aircraft, liquid pipeline transportation, power equipment, biomedicine, and so on, has become an important research topic.[10−14]

Bionic materials with special wettability can achieve drag reduction, and there are many different synthesis methods that can be used to fabricate drag reduction surfaces.[15−20] Wang et

Received: October 4, 2021
Accepted: December 21, 2021
Published: January 3, 2022

https://doi.org/10.1021/acsomega.1c05507
ACS Omega 2022, 7, 2049−2063

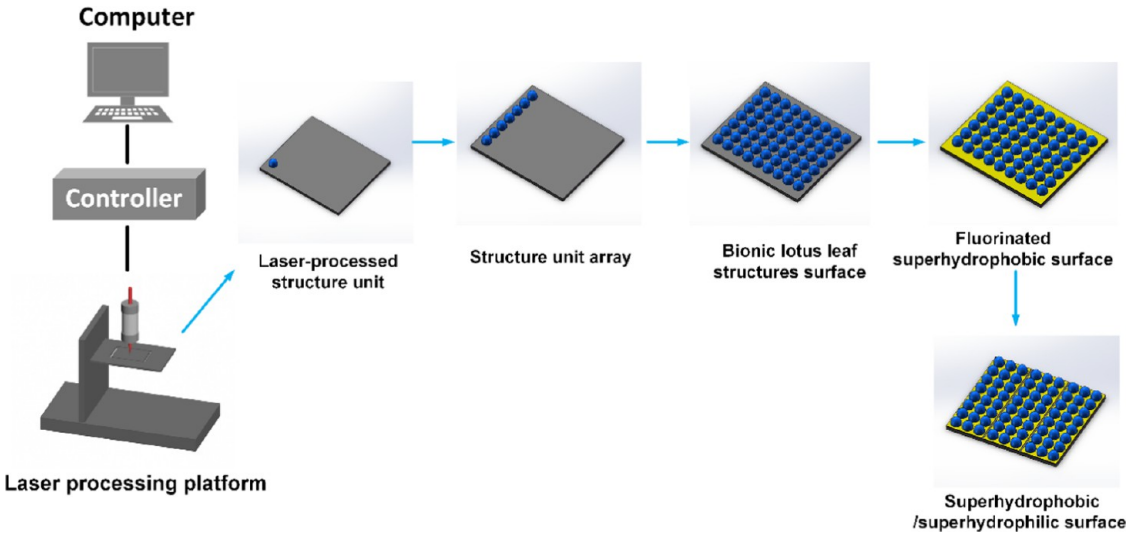

Figure 1. Controllable preparation strategy of BSSs and BSHSs by laser ablation on the Al−Mg substrates.

al. prepared vertical and horizontal interlaced grids as micro/nanostructures for superhydrophobic surfaces to maintain a drag reduction ratio of 13%.[21] Luo et al. used the template method to prepare bionic shark skin with low viscous resistance surfaces at a drag reduction ratio of 12%.[22] Solomon et al. demonstrated the drag reduction mechanism by modeling the effect of lubricant viscosity ratio on fluid resistance in laminar flows.[23] However, most of the fabrication methods, such as emulsion and dispersion polymerization, template forming, and spray, have application limitations. The superhydrophobic surface morphology and wettability prepared by chemical methods are not easy to be accurately controlled, and material failure is inevitable.[24−26] Nanosecond laser scanning ablation with simulation models can accurately design and control a variety of patterned micro/nanostructures with special wettability for optimal performance. Compared with the traditional preparation methods, laser ablation is a pollution-free and environmentally friendly cleaning technology and almost does not cause significant damage to the surface of the substrate. It also has the advantages of convenient processing, good stability, and high-degree automation.[27−31] The morphology, size, and distribution of micro/nanostructures can regulate and control superwettability. Bionic fish scales, horizontal strips of bionic rice leaves, bionic butterfly wings, and other special micro/nanostructures have anisotropy. The surfaces of these bionic structures have been widely studied. The fabricated superhydrophobic surfaces can achieve a certain drag reduction effect.[32−36] Wu et al. proved that the drag reduction effect of the bionic superhydrophobic surface at a flow rate of 0.66 m/s was at the optimum level and that the drag reduction rate was 2.805%.[37] The changing trend of drag reduction rate decreases with an increase of the flow velocity because the friction resistance increases gradually and the air bubble layer on the surface loses rapidly.

The air layer at the solid−liquid interface of the micro/nanostructures on a superhydrophobic surface can reduce the area of liquid−solid direct contact and convert it into part of gas−liquid contacts, which reduces the resistance of the fluid in the boundary layer and increases the fluid velocity. This achieves a drag reduction effect.[38] However, the trapped air layer is destroyed by fluid shear stress, resulting in the instability of the superhydrophobic surface. Under the conditions of bubbles disappearing, external force disturbance, fault of construction, and phase transformation, the drag reduction effect will be impaired when the surface changes from the Cassie state to the Wenzel state. Some researchers have proposed a continuous forced injection of air to maintain a layer of air on a solid surface underwater for drag reduction.[39,40] With the increase of flow velocity, the instability of the fluid boundary layer caused by the loss of a large number of air bubbles broke the drag reduction of the superhydrophobic surface. As a consequence, building a stable air layer on the superhydrophobic surface can maintain a good drag reduction effect at high velocities.

Herein, we propose an efficient strategy to fabricate the controllable patterned bionic superhydrophobic surfaces (BSSs) and bionic superhydrophobic/hydrophilic surfaces (BSHSs) inspired by the convex array micro/nanostructures of lotus leaves. A nanosecond laser ablation method was used to prepare the patterned superhydrophobic surfaces with alternated hydrophilic strips on an aluminum−magnesium alloy substrate. Enhanced superwettability and sliding of BSSs can be obtained by regulating the patterned surface parameters. The alternated hydrophilic strips of BSHSs can build a large energy barrier on the superhydrophobic surface as a wet phase step and then strongly fix the air/water/solid three-phase contact line. Air bubbles attached to the hydrophilic zones are captured to maintain a stable drag reduction effect at high velocities. We used COMSOL to build three-dimensional simulation models to accurately calculate and elucidate the stable and improved drag reduction of BSSs and BSHSs in laminar flows, and we verified the experimental results. The friction resistance and drag reduction ratio were calculated by multiphase flow phase field and surface integral methods. The simulation analysis chose the optimal solution of BSSs and BSHSs. A facile friction resistance measuring equipment is used to test the drag reduction ratios at different flow velocities. This research will improve the superwetting and sliding properties of patterned bionic special wettability surfaces and enhance the stability of drag reduction at high velocities. It has application prospects in the field of reducing energy intensity, drag losses, directional transport of liquids, and ship engineering.

https://doi.org/10.1021/acsomega.1c05507
ACS Omega 2022, 7, 2049−2063

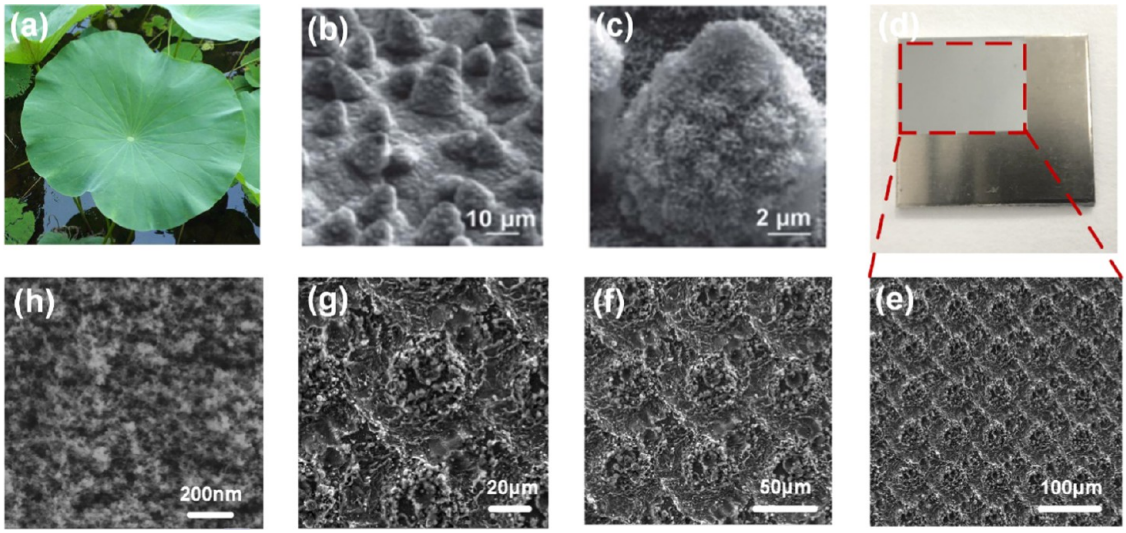

Figure 2. (a) Photograph of a lotus leaf (Photograph courtesy of "Jinglin Zhang." Copyright 2018; and it is a free domain). (b, c) SEM images of micro/nanostructures on the lotus leaf surface and enlarged SEM images (adapted with permission from ref 33). (d) As-prepared BSS sample. (e−h) Enlarged SEM images of the laser-treated BSS of the bionic lotus leaf micro/nanostructured unit with a diameter of 40 μm under various magnifications.

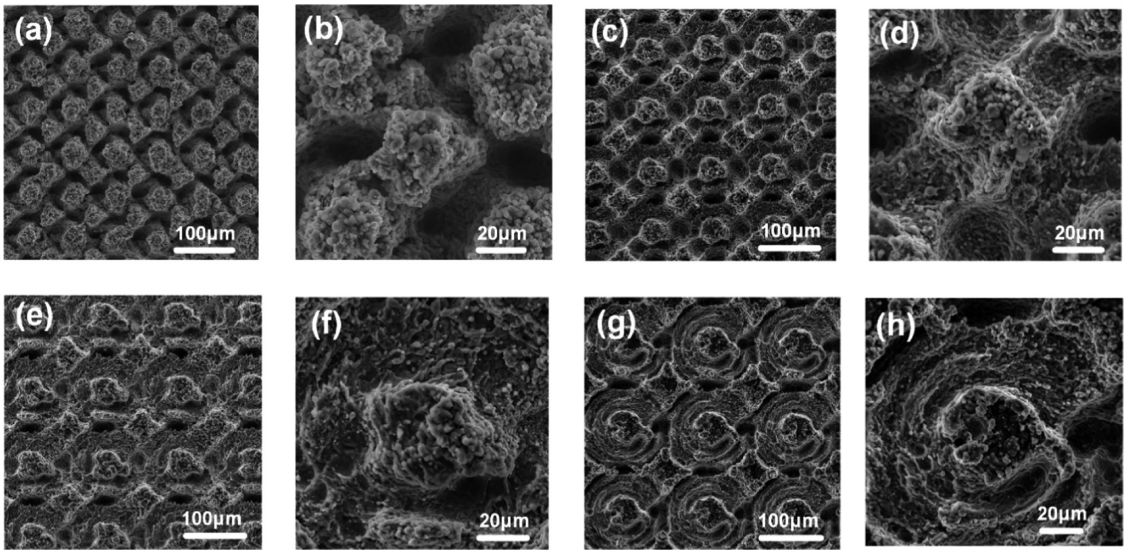

Figure 3. (a, b) SEM images of the BSS sample with a unit diameter of 20 μm. (c, d) SEM images of a sample with a unit diameter of 50 μm. (e, f) SEM images of a sample with a unit diameter of 60 μm. (g, h) SEM images of a sample with a unit diameter of 70 μm.

PREPARATION OF BSSS AND BSHSS

A controllable preparation strategy for BSSs and BSHSs is shown in Figure 1. Before the laser ablation process, the samples were degreased in acetone, alcohol, and a 0.1 M oxalic acid solution, washed in an ultrasonic cleaner, and dried in a drying oven at 120 °C. An area of 1.75 × 3.5 mm^2 of each sample was ablated. Deionized water was used to clean the samples and dried for 30 min. In the end, the samples were immersed in fluoroalkylsilane (FAS, 1H,1H,2H,2H-peruorooctadecyltrichlorosilane) for 1.5 h and dried in a drying oven at 80 °C. The laser etching patterns and hydrophilic strips were established according to CAD models. Each substrate was horizontally placed on the working platform ablated by a vertical laser beam.

RESULTS AND DISCUSSION

Figure 2a−c shows the photograph of a lotus leaf and scanning electron microscopy (SEM) images of the convex micro/nanostructures on the lotus leaf surface at different magnifications. A BSS sample is fabricated on an aluminum−magnesium alloy substrate by laser ablation, as shown in Figure 2d. Each bionic lotus leaf micro/nanostructured unit with a diameter of 40 μm is constructed on the BSHS sample. The micro/nanostructure is similar to that of a real lotus leaf compared to those with other diameters in Figure 2e−g. We used the laser ablation method for each unit along the edge of the bionic lotus leaf micro/nanostructure, and then the convex micro/nanostructure began to take shape in the middle. The nanoscale particulate melts on the surface produced by laser ablation are shown in Figure 2h. The surface roughness and superhydrophobicity can be enhanced by the micro/nano-

https://doi.org/10.1021/acsomega.1c05507
ACS Omega 2022, 7, 2049−2063

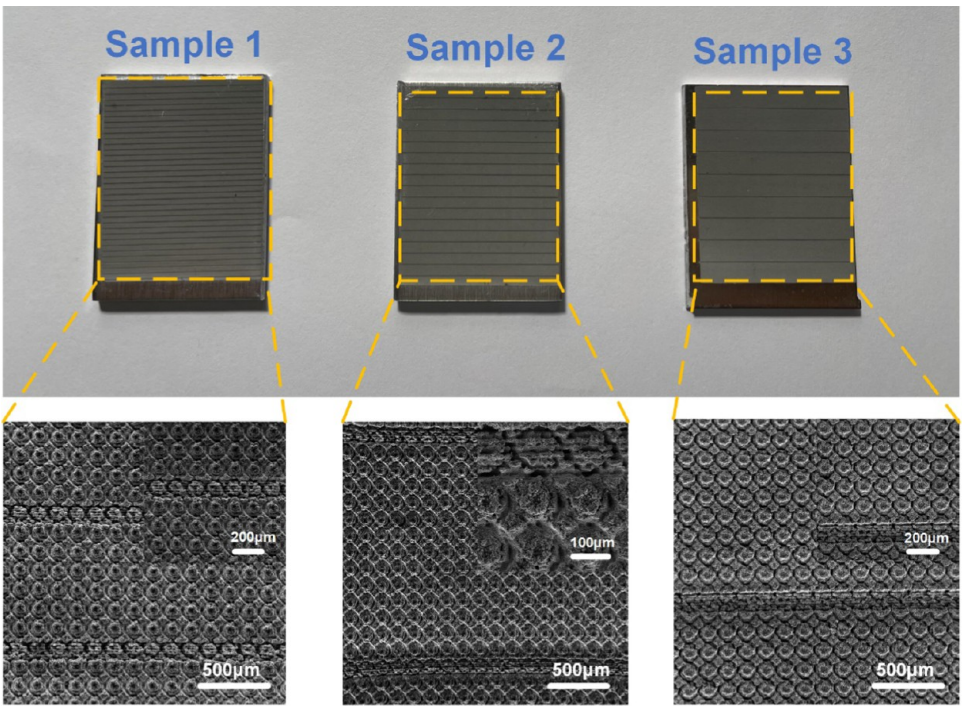

Figure 4. SEM images of three BSHS samples with hydrophilic strip spacings of 1 mm (sample 1), 2 mm (sample 2), and 3 mm (sample 3).

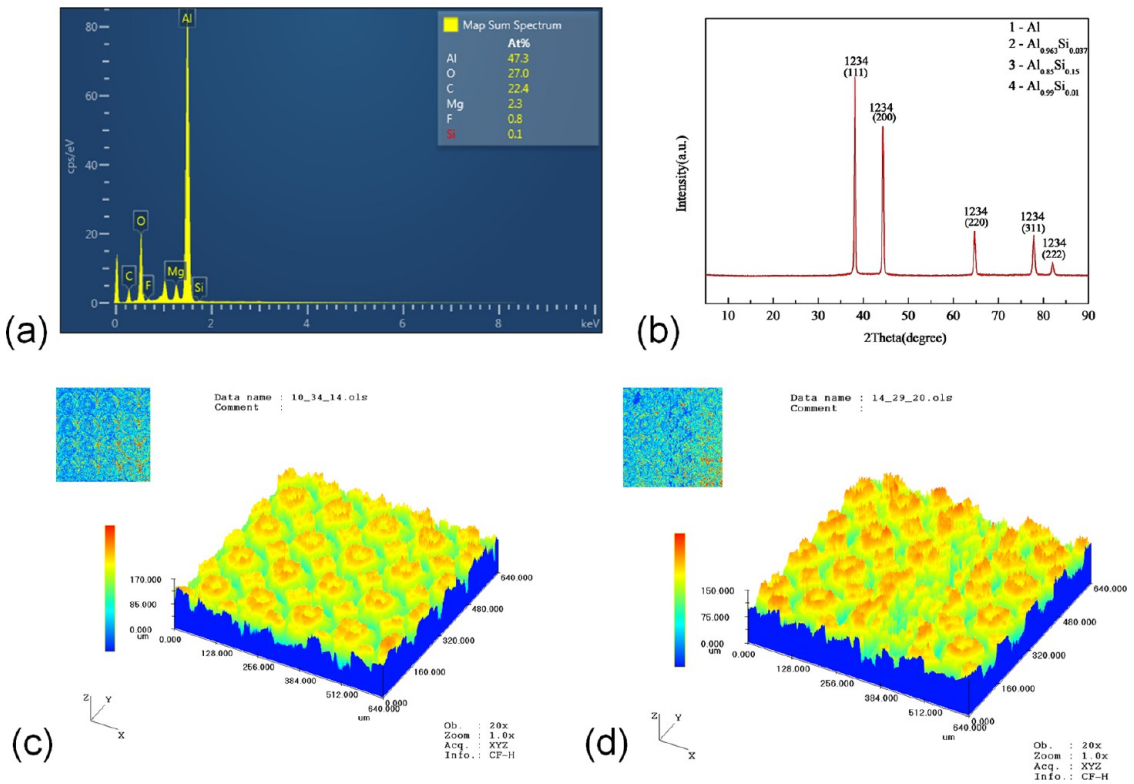

Figure 5. (a) EDS pattern of the BSS sample with a micro/nanostructured unit diameter of 40 μm. (b) XRD pattern of the BSS sample. (c) Three-dimensional morphology of the BSS sample. (d) Three-dimensional morphology of the BSHS sample.

structures of BSSs. The drag reduction effect will increase with an increase in superhydrophobicity.

The SEM images of the four as-prepared BSS samples with unit diameters of 20, 50, 60, and 70 μm are shown in Figure 3a–h under various magnifications. The surface roughness decreases with the increase of the diameter. When the unit diameter is 20 μm, the micro/nanostructured units are similar to the real convex surface of lotus leaves. But, the structural units are irregular, and the size of the bulge units is smaller than that in the structural unit with a diameter of 40 μm. When the diameter of the structural unit is increased to 50 μm, the shape of each unit can still be seen clearly but the spacing

https://doi.org/10.1021/acsomega.1c05507
ACS Omega 2022, 7, 2049−2063

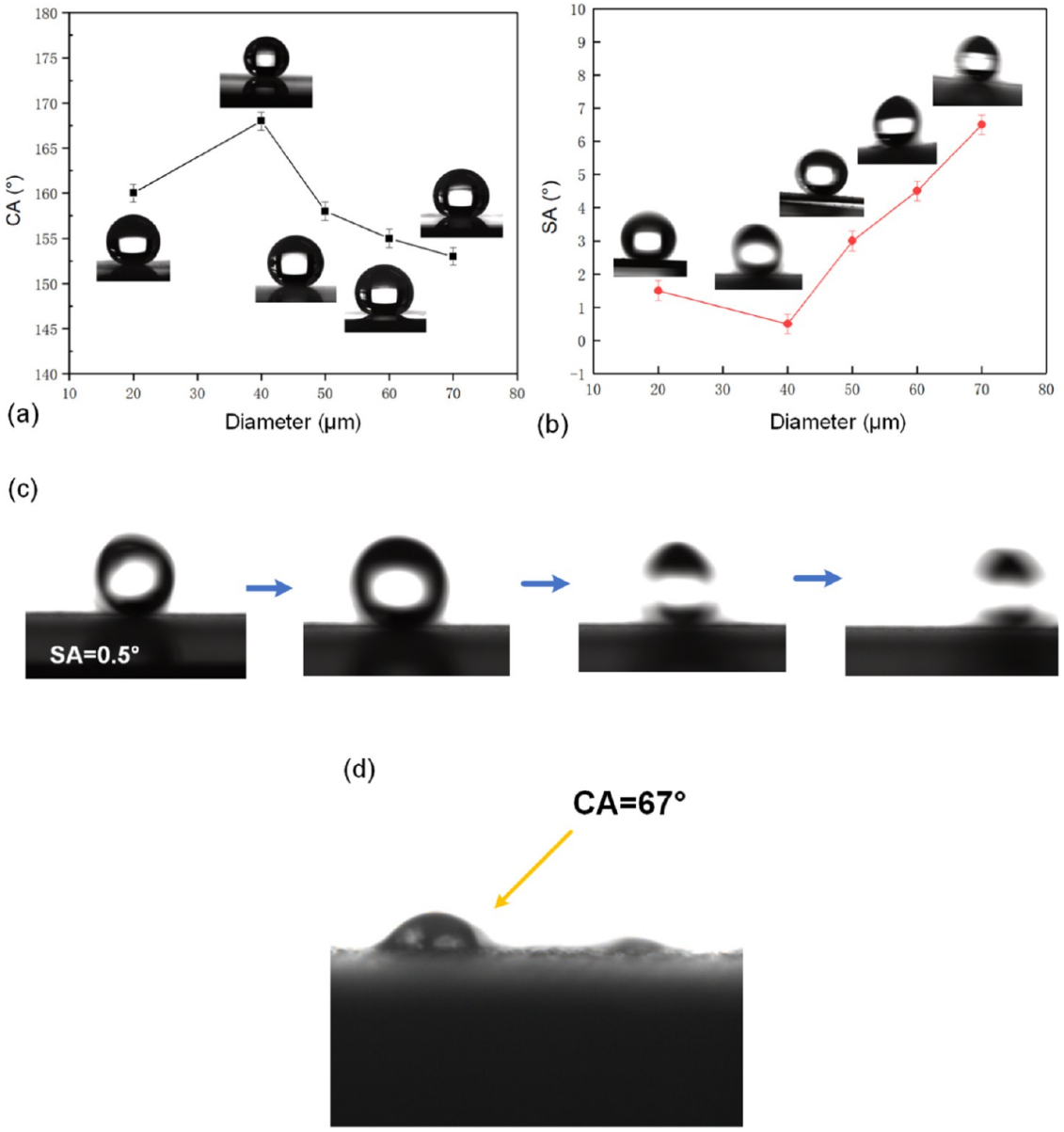

Figure 6. (a) CAs and (b) SAs of the BSS samples with various diameters. (c) Video frames of continuously sliding water droplets on the BSS sample with a diameter of 40 μm. (d) Water contact angle on a hydrophilic area.

between each unit is increased, and the height of the bulge is significantly decreased. At this time, the surface roughness is decreased compared to that of the structural unit with a diameter of 40 μm. As the diameters are increased to 60 and 70 μm, regular and tight protruding structures can no longer be formed. The spacing between units is larger and the protruding height is lower. The surface roughness will decrease when the diameter is greater than 40 μm. The diameter of 40 μm affords the best values for the surface morphology and surface roughness. The superhydrophobicity can be improved by high roughness and it benefits the drag reduction effect of BSSs.

The SEM images of the three as-prepared BSHS samples with a hydrophilic strip spacing of 1, 2, and 3 mm are shown in Figure 4. The bionic micro/nanostructured unit diameter is 40 μm, and each hydrophobic strip width is 50 μm. To control variables, the surfaces prepared on each substrate have the same laser-etched area as sample 1, sample 2, and sample 3. The best hydrophilic strip spacing and the improved stable drag reduction effect for the BSHS are obtained by simulation analysis and drag reduction experiments.

The EDS pattern of the BSS sample with a bionic lotus leaf micro/nanostructured unit diameter of 40 μm is shown in Figure 5a. The chemical compositions and contents of the BSS sample are as follows: Al (47.3%), O (27%), C (22.4%), F (0.8%), Mg (2.3%), and Si (0.1%). An Empyrean diffractometer was used to test the X-ray diffraction (XRD) pattern results. It analyzed the composition of the BSS sample. The XRD pattern of the BSS sample is shown in Figure 5b. Diffraction peaks of the BSS include Al [PDF: 04-003-2966], $Al_{0.963}Si_{0.037}$ [PDF: 04-003-7126], $Al_{0.85}Si_{0.15}$ [PDF: 04-003-7125], and $Al_{0.99}Si_{0.01}$ [PDF: 04-001-2511]. The five strong peaks located at 38.583, 44.787, 65.074, 78.139, and 82.480° are ascribed to the (111), (200), (220), (311), and (222) planes, respectively. Al and the solid solution of Al and Si are the main compositions of the BSS sample. A 3D interference contour tester is used to measure the surface roughness of the

https://doi.org/10.1021/acsomega.1c05507
ACS Omega 2022, 7, 2049−2063

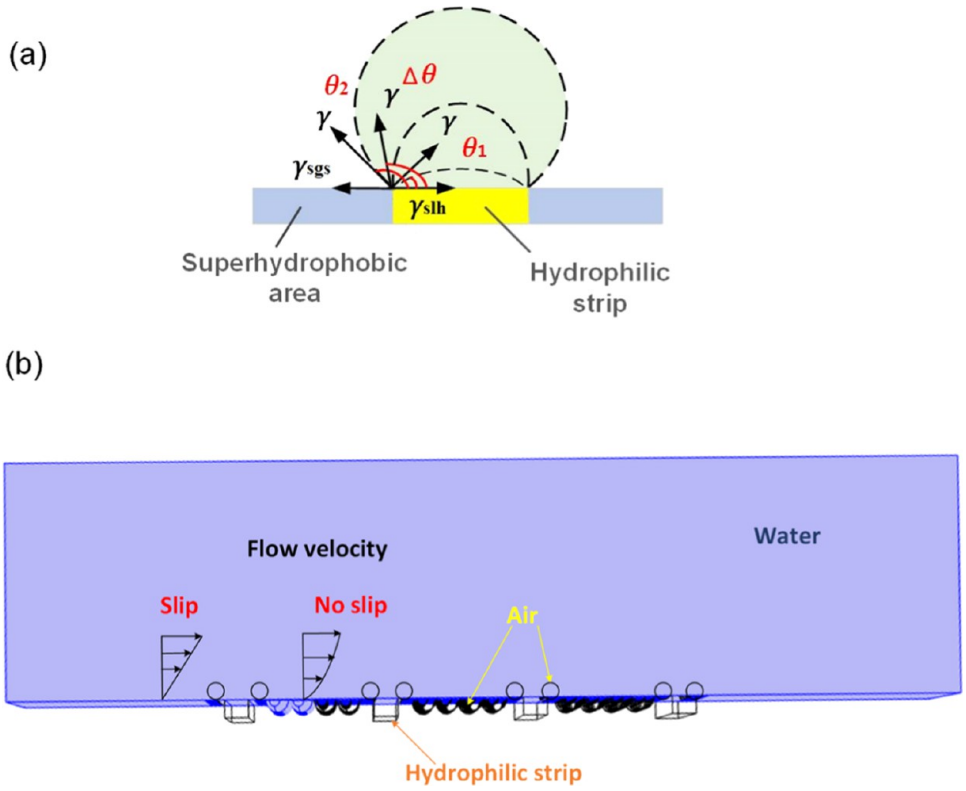

Figure 7. (a) Schematic of the stress balance condition of the three-phase contact line at the superhydrophobic/hydrophilic surface (adapted with permission from ref 41). (b) Bubble blocking and interface slippage mechanism of a BSHS simulation model at the flow impact.

BSS and BSHS samples. Figure 5c,d shows the typical 3D morphologies of the BSS and BSHS samples. The prepared BSS and BSHS samples exhibit a homogeneous distribution. The average mean square roughnesses (R_a) of the BSS and BSHS samples are 3.3886 and 4.788 μm, respectively. The maximum height fluctuation (R_z) values of BSS and BSHS samples are 61.1984 and 73.7428 μm, respectively. Many regular bionic lotus leaf micro/nanostructures and hydrophilic strips are present on the surface of the BSS and BSHS samples. The local convex rough surface can improve superhydrophobicity.

Figure 6a shows the diagram of the water contact angle (CA) as a function of the structure unit diameters of BSSs. When the diameter is 20 μm, the CA is 160°, and when the diameter is 40 μm, the CA improves to 168° at a maximum. The change in CAs may be attributed to the difference in the surface morphology of BSSs with different diameters of the unit. After laser ablation, granular melt protrusions produce smaller rough nanostructures. When the diameter is 40 μm, the CA is greater than those for units with diameters of 50−80 μm shown in Figures 2 and 3. Therefore, the CA for units with 40 μm diameter is larger than those for 50−80 μm. Deep holes along the micro/nanostructure units of 20 μm are produced by laser ablation, resulting in inhomogeneity of the surface morphology. It indicates that the surface with a unit of too small diameter will form a deeper hole by laser etching, and it is not the best surface morphology and contact angle. The CAs decrease with the increase of diameters. When the diameters increase to 50, 60, 70, and 80 μm, the CAs decrease to 158, 155, and 153°, respectively. When the diameters are large, the spacing between each microstructure unit increases, each convex structure becomes smaller and irregular, and the heights decrease compared with those of 20 and 40 μm. The paths and quantities of laser decrease when they etch the same number of micro/nanostructure units. Fewer convex nanostructures of molten materials are produced by the same amount of laser energy. The lack of molten materials and smaller irregular units decrease the superhydrophobicity of BSSs. The surface with a diameter of 40 μm has an optimal size, shape, and roughness for the best superhydrophobicity. The variation tendency of water sliding angle (SA) under various diameters is similar to that of water CA. The diameter is the key parameter to determine the sliding property of BSSs, as shown in Figure 6b. The changing trend of SA is that it decreases first and then increases with the increase of diameter, and then it reaches the maximum value at 40 μm. For diameters of 20, 50, 60, 70, and 80 μm, the SAs are 1.5, 3, 4.5, and 6.5°, respectively. The video frames of continuously sliding water droplets on the BSS sample with a diameter of 40 μm are shown in Figure 6c. The smallest SA of 40 μm is 0.5°, which indicates that the surface is more slippery when the micro/nanostructure unit is of the optimal size, shape, and roughness. Figure 6d shows the water CA on a hydrophilic area of the BSS sample with a diameter of 40 μm. The water CA is 67°, which indicates that the hydrophilic strips are hydrophilic. The best roughness of micro/nanostructures will enhance the superhydrophobicity of the BSS and further promote the drag reduction effect. A BSS with a diameter of 40 μm has the best superhydrophobicity as a test and analyzed the sample for the drag reduction property. The same parameters are used for the preparation of the BSHS samples.

The hydrophilic strips have some effect on the three-phase contact line for the superhydrophobic/hydrophilic surface. The three-phase contact line is bound at the boundary of the

https://doi.org/10.1021/acsomega.1c05507
ACS Omega 2022, 7, 2049−2063

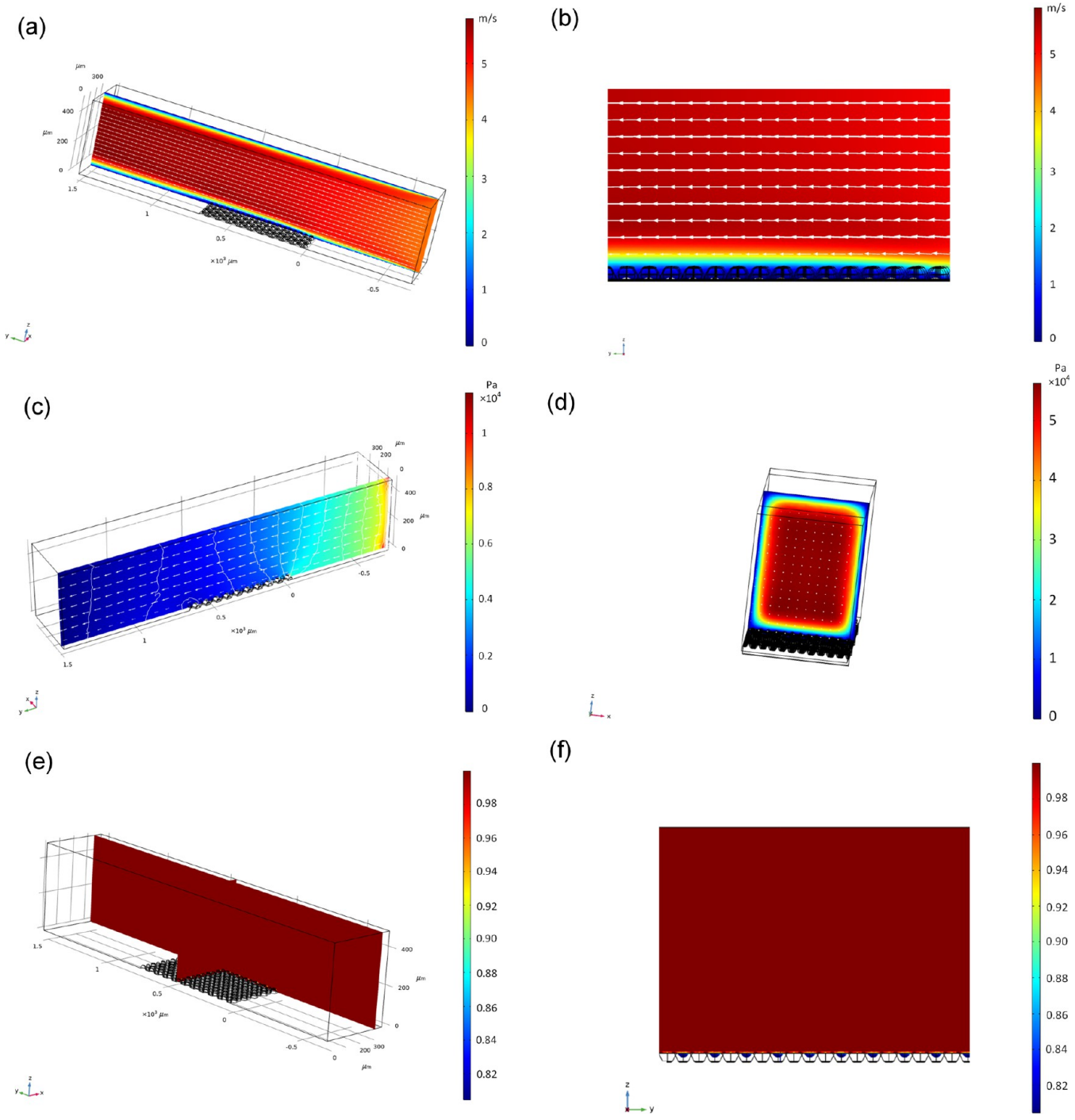

Figure 8. Simulation analysis of the BSS. (a, b) Velocity contour and the partially enlarged photograph of the cross section in the $y-z$ plane; (c, d) static pressure distribution in the near-wall area and the cross-sectional photograph in the $x-z$ plane; (e, f) liquid−gas volume fraction distribution and its partially enlarged photograph on the cross section in the $y-z$ plane.

surface. A contact angle hysteresis phenomenon is shown in Figure 7a. The contact line of the liquid does not change as it reaches the superhydrophobic/hydrophilic interface regions. As the contact angle of the droplet increases, the three-phase contact line always keeps the force in a balanced state. The force balance equation of the three-phase contact line at the hydrophilic and superhydrophobic boundary is[41]

$$\gamma_{sgs} - \gamma_{slh} \le \gamma \cos \theta' \le \gamma_{sgh} - \gamma_{slh} \quad (1)$$

where θ' is the apparent CA, γ_{slh} and γ_{sgh} are the solid−liquid and solid−gas surface tension on the hydrophilic surface, and γ_{sls} and γ_{sgs} are the solid−liquid and solid−gas surface tension on the superhydrophobic surface. The CA hysteresis extent of superhydrophobic/hydrophilic surfaces is[41]

$$V\theta = \theta_{max}{}' - \theta_1 \approx \theta_2 - \theta_1 \quad (2)$$

where θ_1 and θ_2 are the CAs on the superhydrophobic/hydrophilic surface.

https://doi.org/10.1021/acsomega.1c05507
ACS Omega 2022, 7, 2049−2063

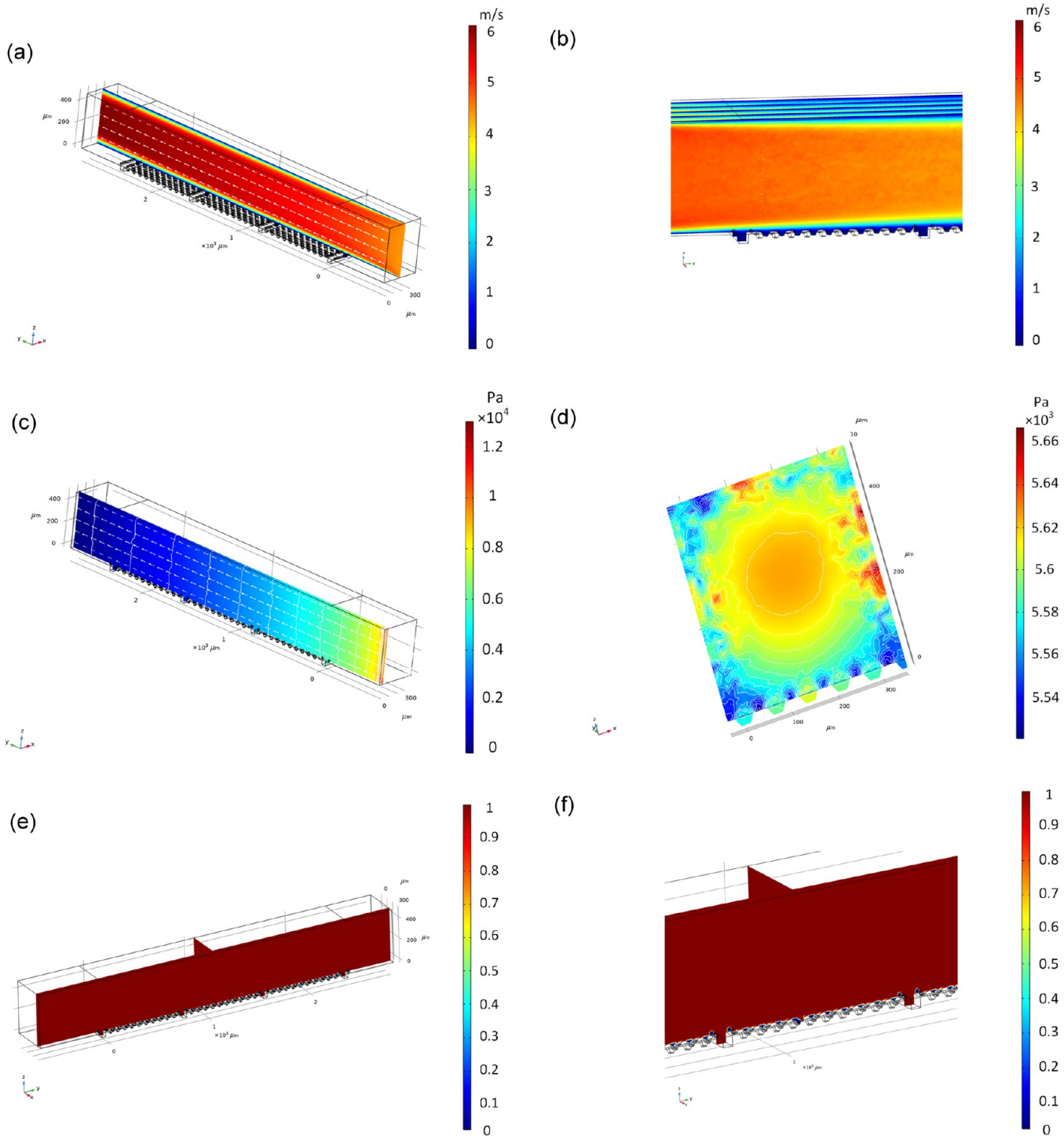

Figure 9. Simulation analysis of the BSHS. (a, b) Velocity vector and the partially enlarged photograph of the cross section in the $y-z$ plane; (c, d) static pressure distribution in the near-wall area and the cross-sectional photograph in the $x-z$ plane at the pressure outlet; (e, f) liquid−gas volume fraction distribution and the partially enlarged photograph on the cross section in the $y-z$ plane.

It has a similar stress state of the air layer on the solid in air and underwater. Therefore, when bubbles are attached to BSHS underwater, the theory can also be applied for the stress balance condition of the three-phase contact line. BSHSs can bind to the three-phase contact line underwater. When the gas contact line moves outward from the superhydrophobic surface to the hydrophilic interface region, it is bound by a partial CA hysteresis. An air layer is attached on the superhydrophobic surface.[42,43] Interface slippage exists on the hydrophilic and superhydrophobic structures with a sealed stable air layer. Friction resistance will reduce by interface slippage. The wetting step can be constructed by laser ablation of hydrophilic strips on the BSHS by adjusting the spacing of hydrophilic strips reasonably. The bound three-phase contact line captures the air bubbles sheared away and locks them and attaches along the hydrophilic strips to maintain the stable drag reduction effect at a high flow velocity. Bubble blocking and interface slippage mechanism of a BSHS simulation model at

https://doi.org/10.1021/acsomega.1c05507
ACS Omega 2022, 7, 2049−2063

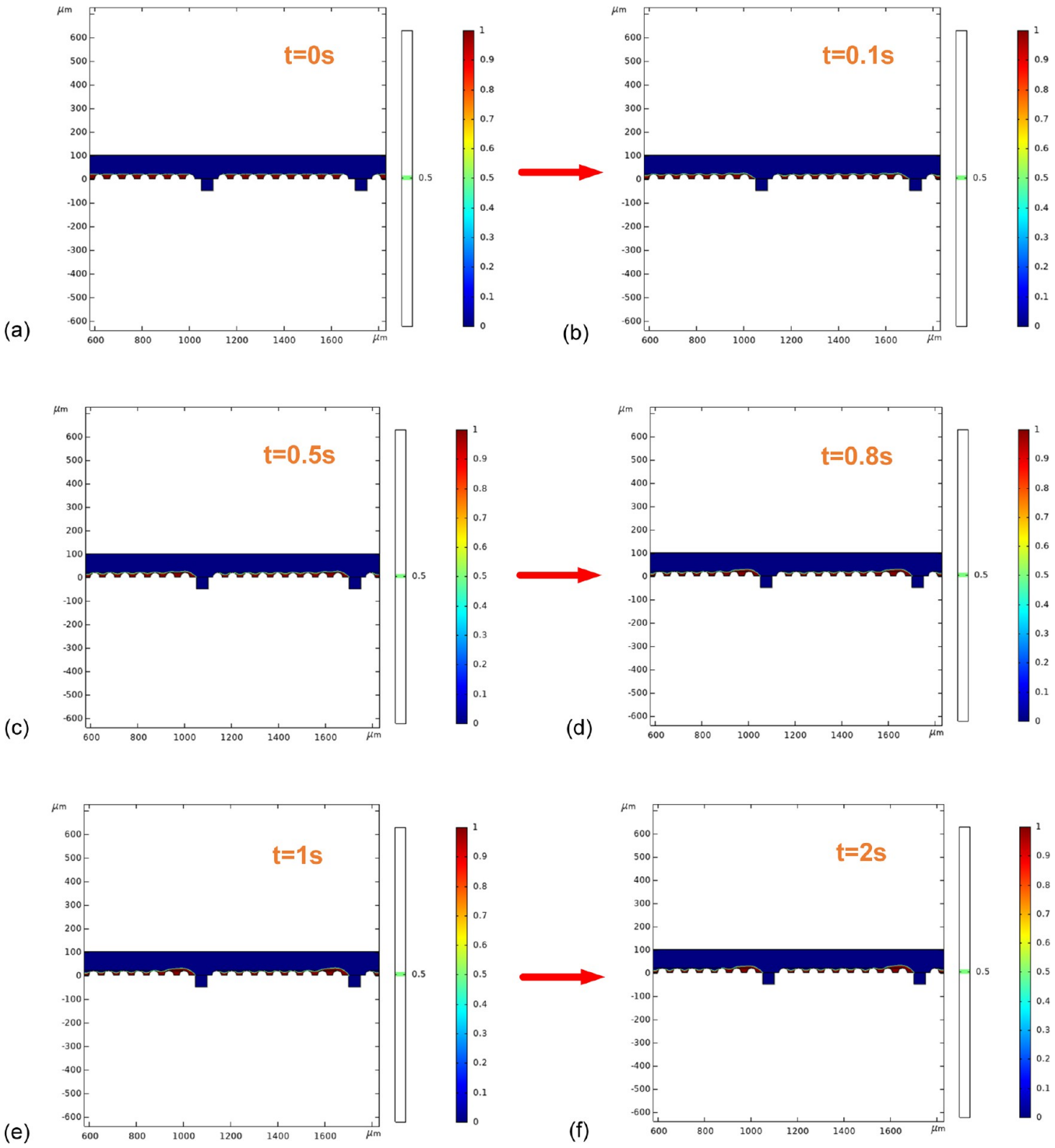

Figure 10. (a–f) Dynamic process of air layer stable existence and interface slippage of the two-dimensional BSHS model.

the flow impact are shown in Figure 5b. The air bubble layer contains the air layer existing near the hollow micro/nanostructures of the BSHS and the sealing air bubbles around the hydrophilic strips. The presence of an air layer makes the liquid–gas interface partially replace the original liquid–solid interface, resulting in interface slippage and reducing the original friction resistance of the solid–liquid interface. Interface slippage is the main factor to improve the drag reduction effect.

We use COMSOL by a three-dimensional finite element method to establish the BSS (Figure 8) and BSHS (Figure 9) simulation models at a flow velocity. The models are based on the fluid–solid coupling physical field and the volume of fluid method. The left inlet and right outside of the model are velocity and pressure, respectively. The pressure is set to 0. The upper surface of the computational domain is set as the untreated surface for comparison. The superhydrophobic surface with the same bionic micro/nanostructures is the lower surface as the prepared BSS sample. The other model

https://doi.org/10.1021/acsomega.1c05507
ACS Omega 2022, 7, 2049−2063

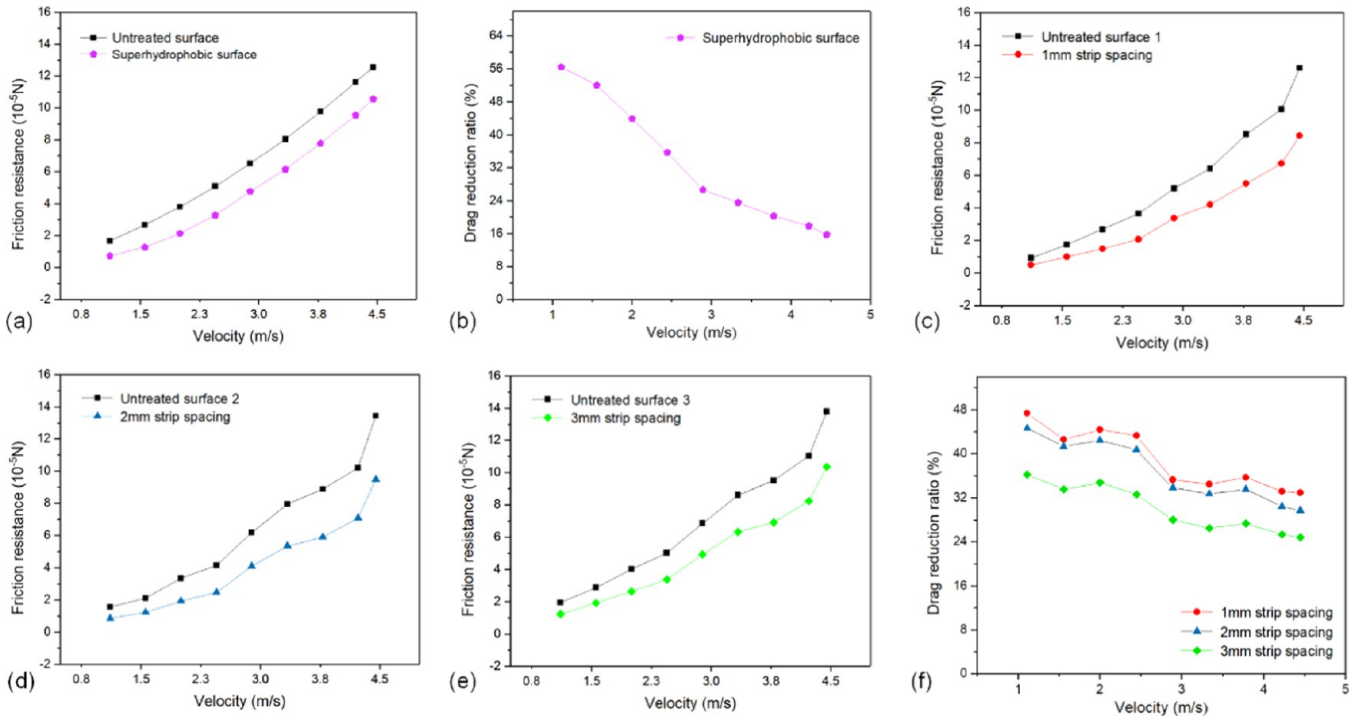

Figure 11. (a) Friction resistance of the untreated surface and the BSS model at different velocities. (b) Drag reduction ratios of the BSS model at different velocities. (c–e) Friction resistance of the untreated surfaces and BSHS models with different hydrophilic strip spacings at different velocities. (f) Drag reduction ratios of the BSHS models with different hydrophilic strip spacings at different velocities.

simulates the superhydrophobic/hydrophilic surface as the prepared BSHS sample. Based on the Reynolds equation, the laminar flow field under a stable condition is simulated numerically. The characteristic height of the calculated domain is 200 μm. In accordance with the best superhydrophobicity parameters, the height and diameter of the micro/nanostructured unit are 30 and 40 μm, respectively, while the hydrophilic strip spacings are 1, 2, and 3 mm, and the hydrophobic strip width is 50 μm.

The simulation models are described by the continuity equation of fluid motion with respect to solid as follows

$$\frac{\partial u}{\partial x} + \frac{\partial v}{\partial y} + \frac{\partial w}{\partial z} = 0 \tag{3}$$

The gravitational force is neglected on the micron scale, and so the momentum equations are

$$\begin{aligned}
&\rho\left(u\frac{\partial u}{\partial x} + v\frac{\partial u}{\partial y} + w\frac{\partial u}{\partial z}\right) \\
&\quad = -\frac{\partial p}{\partial x} + \mu\left(\frac{\partial^2 u}{\partial x^2} + \frac{\partial^2 u}{\partial y^2} + \frac{\partial^2 u}{\partial z^2}\right) \\
&\rho\left(u\frac{\partial v}{\partial x} + v\frac{\partial v}{\partial y} + w\frac{\partial v}{\partial z}\right) = -\frac{\partial p}{\partial y} + \mu\left(\frac{\partial^2 v}{\partial x^2} + \frac{\partial^2 v}{\partial y^2} + \frac{\partial^2 v}{\partial z^2}\right) \\
&\rho\left(u\frac{\partial w}{\partial x} + v\frac{\partial w}{\partial y} + w\frac{\partial w}{\partial z}\right) \\
&\quad = -\frac{\partial p}{\partial z} + \mu\left(\frac{\partial^2 w}{\partial x^2} + \frac{\partial^2 w}{\partial y^2} + \frac{\partial^2 w}{\partial z^2}\right)
\end{aligned} \tag{4}$$

where u, v, and w are the fluid velocities (m/s) in the x, y, and z directions, respectively, μ is the dynamic viscosity (Pa·s), ρ is the density (kg/m^3), and p is the pressure (Pa).[40]

Figure 8 shows the simulation analysis of the BSS at 2 m/s. The overall velocity contour distribution and a partially enlarged photograph of velocity vector distribution in the near-wall area on the cross section in the y–z plane are shown in Figure 8a,b. As the water flows through, there is an obvious change in the velocity gradient on the gas–liquid interface. As the friction resistance increases, the fluid velocity near the upper wall surface and at the liquid–solid interface near the lower wall gradually decreases, and the fluid velocity at the gas–liquid interface with micro/nanostructures is obviously higher than that at the solid–liquid interface. The velocities of the bionic lotus leaf micro/nanostructures near the wall (the blue and green areas) are greater than those at the solid–liquid interface. BSSs with the bionic lotus leaf micro/nanostructures can capture an air layer to form interface slippage to improve the velocity. Viscous resistance is produced by the velocity gradient near the wall. The bubbles are sealed near the wall to form the liquid–gas interface slippage. It can produce a drag reduction effect. Velocity in the x-direction increases by interface slippage, and then viscous resistance decreases. The total resistance of the BSS consists of viscous resistance and pressure resistance. Compared with the viscous resistance, the pressure resistance is smaller in the order of magnitude and can be ignored. Therefore, the friction resistance is mainly composed of viscous resistance. The BSS can reduce the viscous resistance, improve the flow velocity near the wall, and reduce the resistance. The static pressure distribution near the wall and the cross-sectional photograph in the x–z plane are shown in Figure 8c,d. Compared with the untreated surface, the BSS with micro/nanostructures has a more stable static pressure field, as shown in Figure 8c. The static pressure field

https://doi.org/10.1021/acsomega.1c05507
ACS Omega 2022, 7, 2049−2063

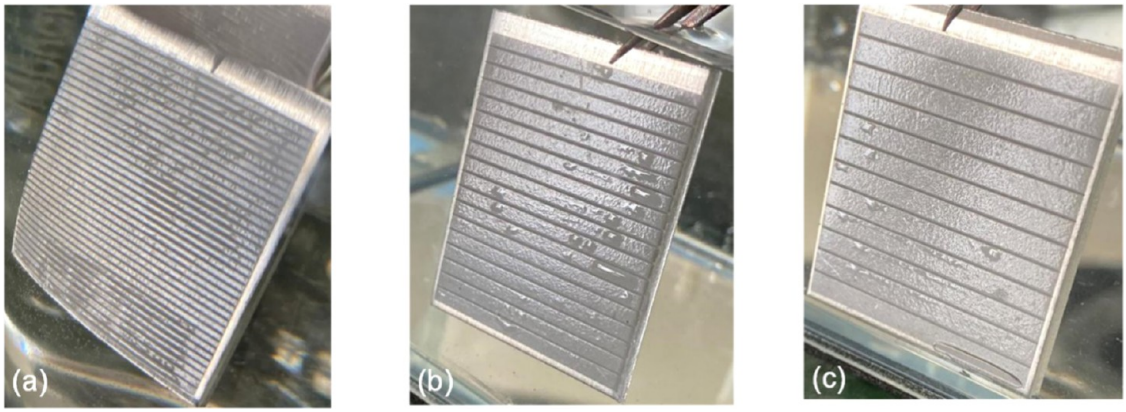

Figure 12. (a−c) Snapshots of sealing air bubbles underwater in three BSHS samples with hydrophilic strip spacings of 1, 2, and 3 mm, respectively.

changes obviously only near the wall, as shown in Figure 8d, and it leads to pressure resistance. Figure 8e,f shows the liquid−gas volume fraction distribution and partially enlarged photograph on the cross section in the $y-z$ plane. Red and blue represent water and gas, respectively. An air layer can be formed near the bionic lotus leaf micro/nanostructure to improve the drag reduction effect of the BSS.

In Figure 9, the simulation analysis indicates that the hydrophilic strips of the BSHS can capture the bubbles to attain a stable drag reduction. The velocity vector and the partially enlarged photograph on the cross section in the $y-z$ plane are shown in Figure 9a,b. When water flows through, the velocity gradient at the gas−liquid interface is influenced by the superhydrophobic/hydrophilic surface with the micro/nanostructures. With the increase of friction resistance, the fluid velocity near the gas−liquid interface is obviously higher than that at the solid−liquid interface. Figure 9c,d shows the static pressure distribution near the wall and the cross-sectional photograph in the $x-z$ plane at the pressure outlet. The static pressure field is simultaneously influenced by the superhydrophobic/hydrophilic surface to produce the pressure resistance. In the pressure outlet section, the superhydrophobic/hydrophilic area near the wall causes the change in the nearby flow field, and the overall stability is in the concentrated area of the velocity far from the wall. Figure 9e,f shows the liquid−gas volume fraction distribution. The liquid exists in the hydrophilic strips. The bubbles are attached to the hydrophilic strips. The BSHS in synergy can achieve a stable drag reduction at high velocities.

Figure 10 and Video S1 show a dynamic process of the stable existence and interface slippage of the two-dimensional BSHS model at a flow velocity of 2 m/s. As the water flows across the BSHS, the air layer always exists and tends to be stably locked around the hydrophilic strips after dynamic changes. The total air layer contains the air bubbles in the micro/nanostructures of the BSHS and the locked air bubbles around the hydrophilic strips. The diameters of the locked air bubbles around the hydrophilic strips trapped on the BSHS are 30 μm in the model. According to the analysis of the final steady-state solution, the air layer is stable. Its role in the slipping water is to create slippage around the hydrophilic strips for drag reduction.

The friction resistance and drag reduction ratios were calculated by the BSS and three BSHS with different hydrophilic strip spacing simulation models at a flow velocity of 2 m/s in Figure 11. The drag reduction ratio θ_s is calculated as follows

$$\theta_s = \frac{f_g - f_l}{f_g} \times 100\% = \frac{f_{gv} - (f_{lv} + f_{lp})}{f_{gv}} \times 100\% \quad (5)$$

where f_{gv}, f_{lv}, and f_{lp} are the total friction resistance values on the untreated surface, viscous resistance, and pressure resistance of the built BSS and BSHS simulation models, respectively.

The friction resistance of the untreated surface and the BSS model at different velocities (1.112−4.448 m/s) is shown in Figure 11a. The friction resistance increases when the flow velocity increases, as shown in Figure 11b. The maximum resistance is 10.5662×10^{-5} N at the highest velocity of 4.448 m/s. The drag reduction ratio decreases gradually with the increase of the flow velocity. The maximum drag reduction ratio is 56.43% at 1.112 m/s. The drag reduction ratio remains above 50% in the range of 1.112−1.557 m/s. When the velocity is greater than 3.7808 m/s, the drag reduction ratio decreases to less than 20%. It indicates that when the velocity is small, the air layer existing on the BSS can remain stable, and so the drag reduction ratio is large; however, when the flow velocity increases gradually, the trapped air bubble layer on the BSS is unstable and sheared away by the water flow, and thus the interface slippage is destroyed and the drag reduction ratios drop rapidly. Therefore, the drag reduction property of BSSs is excellent at a low velocity by the simulation analysis.

The friction resistance of the untreated surfaces and the BSHS models with different hydrophilic strip spacings at various velocities is shown in Figure 11c−e. The same computational area is used to control variables in the model. The friction resistance increases when the hydrophilic strip spacings change from 1 to 3 mm. The drag reduction ratio fluctuates in stages in Figure 11f. When the flow velocity is 1.112−2.4464 m/s, the drag reduction ratio remains above 40%, and then it decreases and remains at about 30% at 2.4464−4.448 m/s under the trend of fluctuation change. The drag reduction ratio declines when the hydrophilic strip spacings increase. There will be a significant reduction in the drag reduction with the hydrophilic strip spacing increasing to a stable value. With a hydrophilic strip spacing of 1 mm, the friction resistance of BSHS is 0.9319×10^{-5} N at the minimum and the drag reduction ratio is 47.37% at the maximum at a velocity of 1.112 m/s. The hydrophilic strips can seal the air

https://doi.org/10.1021/acsomega.1c05507
ACS Omega 2022, 7, 2049−2063

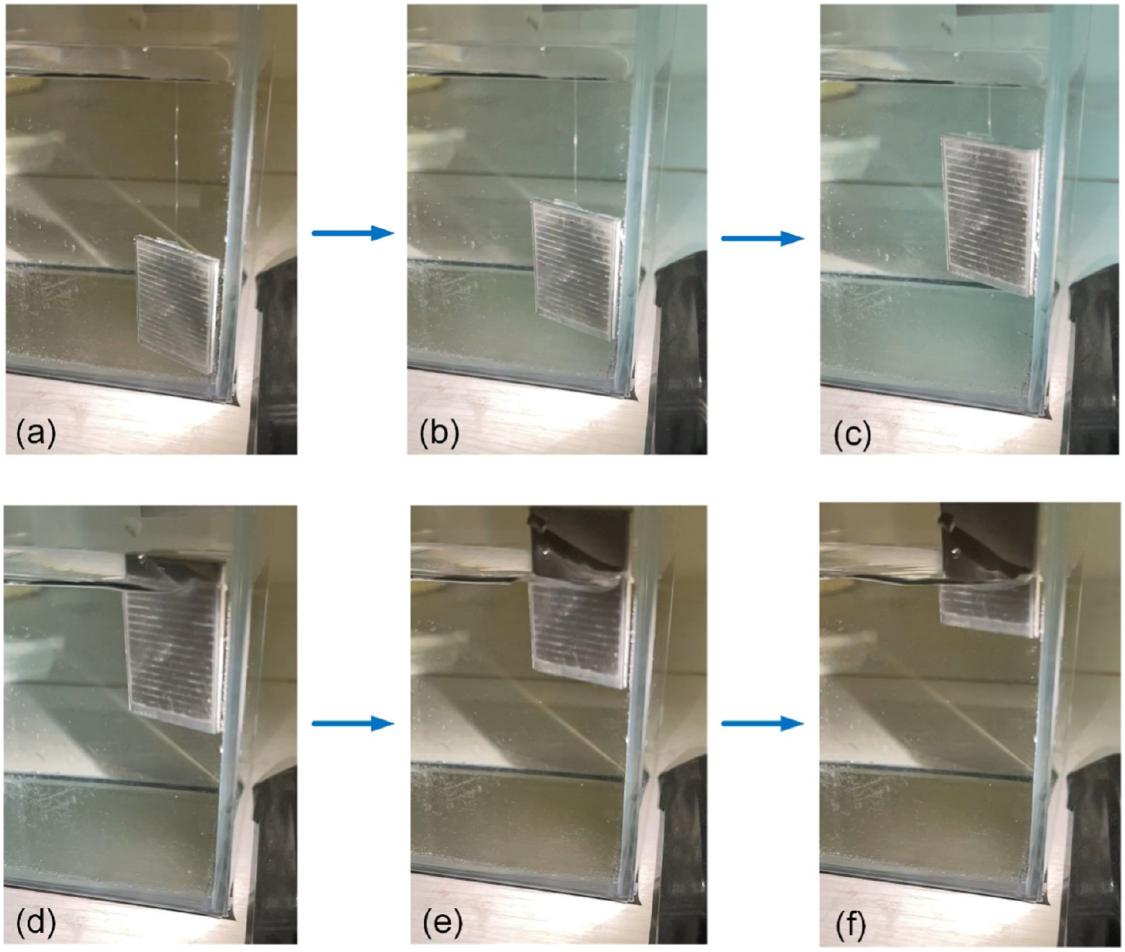

Figure 13. (a–f) Snapshots of the rising process from underwater to air of the BSHS.

bubbles sheared away, and so it can effectively exhibit a stable drag reduction at a high velocity by the simulation analysis. The results show that the BSHS with a hydrophilic strip spacing of 1 mm has the best drag reduction property under the same condition.

Figure 12 shows snapshots of sealing air bubbles underwater in three BSHS samples with hydrophilic strip spacings of 1, 2, and 3 mm in the experiments. The experiment proves that the BSHS has the function of sealing the bubbles near the hydrophilic strips as the flow velocity increases. The smaller the hydrophilic strip spacing, the greater and denser the sealed air bubbles and the better the drag reduction effect. The experimental results are identical to the theoretical simulation.

The rising process from underwater to air of the BSHS is shown in Figure 13 and Video S2. The BSHS sample blocks the bubbles as the acceleration of the velocity increases. The air layer generates and then remains stable during the movement for drag reduction. Therefore, we can be sure of the presence of stable air bubbles in the experiments.

A high-precision self-assembly friction resistance measuring equipment was built to measure the weak friction resistance and the drag reduction property of the samples, as shown in Figure 14. It can also verify the results of simulation analysis. Mechanical, drive, and signal processing modules constitute the test device. Powered by a water pump, water flows through the nozzle and impacts the surface of the test sample and then backflows into the water tank in the experiment. A friction resistance sensor is used to measure the friction resistance at

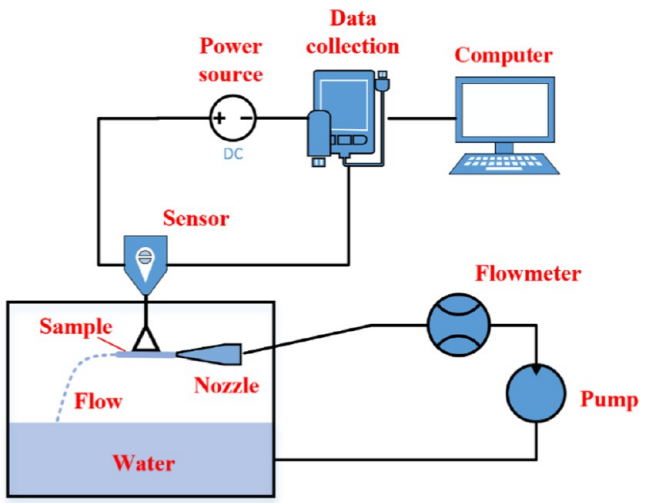

Figure 14. Set of the friction resistance measuring equipment.

the solid–liquid interface on the sample surface. The output signal changes from the strain gauge deformation are collected by the data collection. The corresponding friction resistance value is obtained by conversion. The experimental results are averaged by several measurements.

The BSS and BSHS samples are tested at different velocities. In the experiments, the drag reduction ratio θ_e is calculated as follows

https://doi.org/10.1021/acsomega.1c05507
ACS Omega 2022, 7, 2049−2063

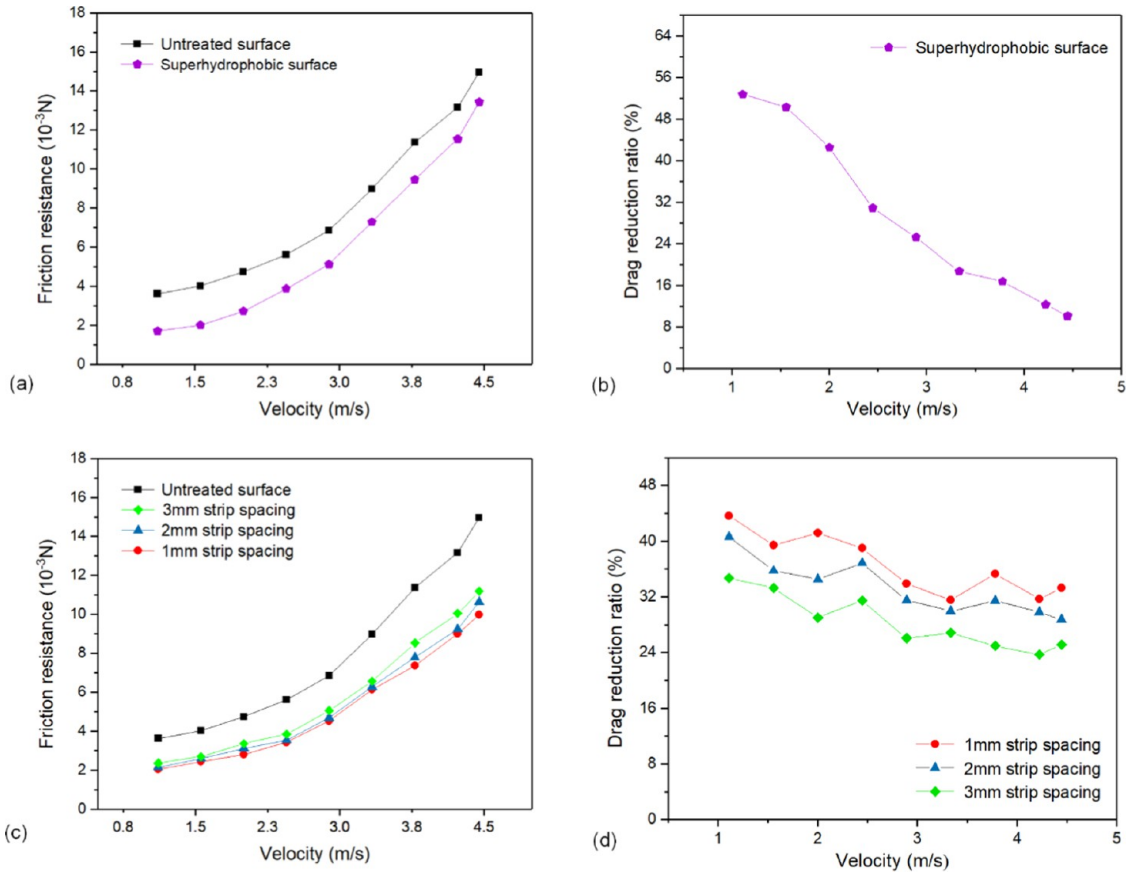

Figure 15. (a) Friction resistance of the untreated surface and the BSS sample at different velocities. (b) Drag reduction ratios of the BSS sample at different velocities. (c) Friction resistance of the untreated surfaces and the BSHS samples with different hydrophilic strip spacings at different velocities. (d) Drag reduction ratios of the BSHS samples with different hydrophilic strip spacings at different velocities.

$$\theta_e = \frac{f_{ge} - f_{le}}{f_{ge}} \times 100\% \quad (6)$$

where f_{ge} and f_{le} are the friction resistance values on the untreated surface and the as-prepared samples, respectively.

A bulk Al−Mg alloy serves as the untreated surface as a control sample and the parameters are controlled in the same conditions. Figure 15a shows that the friction resistance of the untreated surface and the as-prepared BSS sample at different velocities in the drag reduction experiments. The friction resistance increases with the increase of velocity, while the drag reduction ratio decreases with the increase of flow velocity. The drag reduction ratio is 52.76% at the maximum when the friction resistance is 1.7128×10^{-3} N at a velocity of 1.112 m/s, and the minimum value is 10.15% when the friction resistance is 13.4368×10^{-3} N at a velocity of 4.448 m/s in Figure 15b. The overall changing trend of the drag reduction ratio is the same as that of simulation analysis, which shows the correctness of the theory. At a low velocity, the drag reduction effect of the BSS is excellent, while at a high velocity, the impact of water flow affects the air bubble layer sealed by micro/nanostructures, resulting in increasing the friction resistance and reducing the drag reduction effect. In Figure 15c, the variation trend of friction resistance of BSHS samples at different flow velocities is the same as that of BSS. The friction resistance increases when the hydrophilic strip spacing increases. The smallest friction resistances of the BSHS with a hydrophilic strip spacing of 1 mm increase from 2.0432×10^{-3} to 9.9793×10^{-3} N at various velocities. The drag reduction ratios of the BSHS samples with different hydrophilic strip spacings at different velocities are shown in Figure 15d. The drag reduction ratio of the BSHS fluctuates and remains at 40 ± 4% with a velocity less than 2.4464 m/s. As the velocity increases to 4.4468 m/s, the optimal drag reduction ratios can be held nearby 30%. When the flow velocity is 1.112 m/s, the drag reduction ratio is 43.65%. The drag reduction ratios of BSHS with a hydrophilic strip spacing of 1 mm are superior to others at different flow velocities. The BSHS sample with a hydrophilic strip spacing of 1 mm can achieve the best and stable drag reduction properties at high velocities of 2.4468−4.448 m/s. The bionic lotus leaf micro/nanostructures and the hydrophilic strips are significant for the stable drag reduction effect. The experiments verify the correctness of drag reduction simulation models.

CONCLUSIONS

BSSs and BSHSs are ablated by laser on Al−Mg alloys substrates. Bionic lotus leaf micro/nanostructures can improve superhydrophobicity. The nanoscale particulate melts on the surface after ablation, further increasing the surface roughness. When the diameter of the micro/nanostructured unit is 40 μm, the biggest CA is 168°. The smallest SA for 40 μm is 0.5°. The BSS with a diameter of 40 μm has the best superhydrophobicity. The drag reduction ratio is above 50% at low velocities ranging from 1.112 to 2.4468 m/s. The hydrophilic strips pinning the three-phase contact line can form the wetting step. The air bubbles sheared away can be

https://doi.org/10.1021/acsomega.1c05507
ACS Omega 2022, 7, 2049−2063

captured to keep the stable drag reduction at a high velocity. Interfacial slippage formed by the hydrophilic strips and micro/nanostructures can obviously improve the drag reduction effect by an ASHS simulation. The drag reduction ratios can be held nearby 30% at high velocities (2.4468−4.448 m/s). The BSHS with a hydrophilic strip spacing of 1 mm has the optimal stable drag reduction effect. The bionic lotus leaf micro/nanostructures on the superhydrophobic surfaces and the hydrophilic strips are necessary for the stable and high drag reduction properties. The experiments are in accordance with the simulation analysis. Effective stable drag reduction strategies for the BSS and ASHS at a low velocity and a high velocity, respectively, can reduce energy consumption, save cost, and realize the applications such as liquid directional transport, marine vessels, microfluidic devices, and microchannels.

EXPERIMENTAL SECTION

The substrate material is a 6061 aluminum−magnesium alloy with an area of 3.5 × 4.5 cm^2. The ultraviolet laser features a wavelength of 355 nm, a frequency of 100 kHz, a laser energy of 100 mW, and an average power of 15 W in the experiments. The operating temperature of laser scanning ablation for samples was 20 °C.

Contact angles and sliding angles were measured using an optical CA meter system at 20 °C. The surface morphologies were observed with a SEM, Gemini 300. The optical images were obtained using a high-speed video camera (Sony, HDR-CX450). COMSOL was used to build models to simulate the experimental surfaces for demonstrating the drag reduction mechanism, obtaining the optimal solution, and verifying the validity of experiments. A set of measuring equipment was built to measure the friction resistance by the flow impact method.

ASSOCIATED CONTENT

Supporting Information

The Supporting Information is available free of charge at https://pubs.acs.org/doi/10.1021/acsomega.1c05507.

Video S1: Dynamic process of air layer stable existence and interface slippage of two-dimensional BSHS model at a flow velocity of 2 m/s (AVI)

Video S2: Rising process from underwater to air of the BSHS (MP4)

AUTHOR INFORMATION

Corresponding Authors

Liang Chen − *Key Laboratory of Micro-Systems and Micro-Structures Manufacturing, Ministry of Education, Harbin 150001, China; MEMS Center, Harbin Institute of Technology, Harbin 150001, China*; Email: cliang@hit.edu.cn

Xiaowei Liu − *Key Laboratory of Micro-Systems and Micro-Structures Manufacturing, Ministry of Education, Harbin 150001, China; MEMS Center, Harbin Institute of Technology, Harbin 150001, China; State Key Laboratory of Urban Water Resource & Environment, Harbin Institute of Technology, Harbin 150001, China*; Email: lxw@hit.edu.cn

Authors

Wanting Rong − *MEMS Center, Harbin Institute of Technology, Harbin 150001, China*; orcid.org/0000-0002-7257-5546

Haifeng Zhang − *Key Laboratory of Micro-Systems and Micro-Structures Manufacturing, Ministry of Education, Harbin 150001, China; MEMS Center, Harbin Institute of Technology, Harbin 150001, China; State Key Laboratory of Urban Water Resource & Environment, Harbin Institute of Technology, Harbin 150001, China*

Zhigang Mao − *MEMS Center, Harbin Institute of Technology, Harbin 150001, China*

Complete contact information is available at: https://pubs.acs.org/10.1021/acsomega.1c05507

Notes

The authors declare no competing financial interest.

ACKNOWLEDGMENTS

This work was supported by the National Science Foundation of China (No. 61974172) and the Natural Science Foundation of Heilongjiang Province of China (No. LH2020E059).

REFERENCES

(1) Eyring, V.; Köhler, H. W.; Van Aardenne, J.; Lemper, B. Emissions from international shipping: 2. impact of future technologies on scenarios until 2050. *J. Geophys. Res.* **2005**, *110*, No. D17305.

(2) Solomon, B. R.; Khalil, K. S.; Varanasi, K. K. Drag Reduction using Lubricant-Impregnated Surfaces in Viscous Laminar Flow. *Langmuir* **2014**, *30*, 10970−10976.

(3) Wang, J.; Lan, S.; Chen, G. Experimental Study on the Turbulent Boundary Layer Flow over Riblets Surface. *Fluid Dyn. Res.* **2000**, *27*, 217−229.

(4) Koeltzsch, K.; Dinkelacker, A.; Grundmann, R. Flow over convergent and divergent wall riblets. *Exp. Fluids* **2002**, *33*, 346.

(5) Ball, P. Engineering shark skin and other solutions. *Nature* **1999**, *400*, 507.

(6) Shi, F.; Niu, J.; Liu, J.; Liu, F.; Wang, Z.; Feng, X. Q.; Zhang, X. Inside Front Cover: Towards Understanding Why a Superhydrophobic Coating Is Needed by Water Striders. *Adv. Mater.* **2007**, *19*, 2257.

(7) Mchale, G.; Shirtcliffe, N. J.; Evans, C. R.; Newton, M. I. Terminal velocity and drag reduction measurements on superhydrophobic spheres. *Appl. Phys. Lett.* **2009**, *94*, No. 064104.

(8) Dong, H.; Cheng, M.; Zhang, Y.; Wei, H.; Shi, F. Extraordinary drag-reducing effect of a superhydrophobic coating on a macroscopic model ship at high speed. *J. Mater. Chem. A* **2013**, *1*, 5886−5891.

(9) McHale, G.; Newton, M. I.; Shirtcliffe, N. J. Immersed superhydrophobic surfaces: gas exchange, slip and drag reduction properties. *Soft Matter* **2010**, *6*, 714−719.

(10) Viswanath, P. R. Aircraft viscous drag reduction using riblets. *Prog. Aerospace Sci.* **2002**, *38*, 571−600.

(11) Woods, H. Book Reviews: Marine Fouling and Its Prevention. *Science* **1953**, 118−257.

(12) *Industrial Biofouling Detection, Prevention and Control*; In Walker, J.; Surman, S.; Jass, J., Eds.; Wiley: New York, 2000.

(13) Sareen, A.; Deters, R. W.; Henry, S. P.; Selig, M. S. In *Drag Reduction Using Riblet Film Applied to Airfoilsfor Wind Turbines*, 49th AIAA Aerospace Sciences Meeting including the New Horizons Forum and Aerospace Exposition, Orlando, FL, 2011.

(14) Shirtliff, M.; Leid, J. G. *The Role of Biofilms in Device-Related Infections*; Springer-Verlag: Berlin, 2009.

(15) Feng, L.; Li, S. H.; Li, Y. S.; Li, H. J.; Zhang, L. J.; Zhai, J.; Song, Y. L.; Liu, B. Q.; Jiang, L.; Zhu, D. B. Super-hydrophobic surfaces: From natural to artificial. *Adv. Mater.* **2002**, *14*, 1857−1860.

(16) Liu, M. J.; Wang, S. T.; Wei, Z. X.; Song, Y. L.; Jiang, L. Bioinspired Design of a Superoleophobic and Low Adhesive Water/Solid Interface. *Adv. Mater.* **2009**, *21*, 665−669.

(17) Gao, X. F.; Jiang, L. Water-repellent legs of water striders. *Nature* **2004**, *432*, 36.
(18) Liu, K.; Du, J.; Wu, J.; Jiang, L. Superhydrophobic gecko feet with high adhesive forces towards water and their bio-inspired materials. *Nanoscale* **2012**, *4*, 768−772.
(19) Liu, X.; Zhou, J.; Xue, Z.; Gao, J.; Meng, J.; Wang, S.; Jiang, L. Clam's Shell Inspired High-Energy Inorganic Coatings with Underwater Low Adhesive Superoleophobicity. *Adv. Mater.* **2012**, *24*, 3401−3405.
(20) Yang, S.; Ju, J.; Qiu, Y.; He, Y.; Wang, X.; Dou, S.; Liu, K.; Jiang, L. Peanut Leaf Inspired Multifunctional Surfaces. *Small* **2014**, *10*, 294−299.
(21) Wang, B.; Wang, J.; Dou, Z.; Chen, D. Investigation of retention of gases in transverse hydrophobic microgrooved surfaces for drag reduction. *Ocean Eng.* **2014**, *79*, 58−66.
(22) Luo, Y.; Wang, X.; Liu, G.; Wang, J.; Song, W. Anisotropic wetting and fluidic phenomena on biological texture and hydrodynamic experiments testing on different low viscous resistance surfaces. *Adv. Eng. Mater.* **2016**, *18*, 869−876.
(23) Solomon, B. R.; Khalil, K. S.; Varanasi, K. K. Drag reduction using lubricant-impregnated surfaces in viscous laminar flow. *Langmuir* **2014**, *30*, 10970−10976.
(24) Jiao, Y.; Li, C.; Wu, S.; Hu, Y.; Li, J.; Yang, L.; Wu, D.; Chu, J. Switchable Underwater Bubble Wettability on Laser-Induced Titanium Multiscale Micro-/Nanostructures by Vertically Crossed Scanning. *ACS Appl. Mater. Interfaces* **2018**, *10*, 16867−16873.
(25) Yin, K.; Yang, S.; Dong, X. R.; Chu, D. K.; Duan, J. A.; He, J. Robust Laser-structured Asymmetrical PTFE Mesh for Underwater Directional Transportation and Continuous Collection of Gas Bubbles. *Appl. Phys. Lett.* **2018**, *112*, No. 243701.
(26) Yin, K.; Dong, X. R.; Zhang, F.; Wang, C.; Duan, J. A. Superamphiphobic Miniature Boat Fabricated by Laser Micromachining. *Appl. Phys. Lett.* **2017**, *110*, No. 121909.
(27) Yin, K.; Duan, J. A.; Wang, C.; Dong, X. R.; Song, Y. X.; Luo, Z. Micro Torch Assisted Nanostructures' Formation of Nickel During Femtosecond Laser Surface Interactions. *Appl. Phys. Lett.* **2016**, *108*, No. 241601.
(28) Yin, K.; Chu, D. K.; Dong, X. R.; Wang, C.; Duan, J. A.; He, J. Femtosecond Laser Induced Robust Periodic Nanoripple Structured Mesh for Highly Efficient Oil−Water Separation. *Nanoscale* **2017**, *9*, 14229−14235.
(29) Yong, J. L.; Chen, F.; Li, M. J.; Yang, Q.; Fang, Y.; Huo, J. L.; Hou, X. Remarkably Simple Achievement of Superhydrophobicity, Superhydrophilicity, Underwater Superoleophobicity, Underwater Superoleophilicity, Underwater Superaerophobicity, and Underwater Superaerophilicity on Femtosecond Laser Ablated PDMS Surfaces. *J. Mater. Chem. A* **2017**, *5*, 25249−25257.
(30) Lin, Y.; Han, J. P.; Cai, M. Y.; Liu, W. J.; Luo, X.; Zhang, H. J.; Zhong, M. L. Durable and Robust Transparent Superhydrophobic Glass Surfaces Fabricated by A Femtosecond Laser with Exceptional Water Repellency and Thermostability. *J. Mater. Chem. A* **2018**, *6*, 9049−9056.
(31) Yan, H. P.; Rashid, M. R. B.; Khew, S. Y.; Li, F. P.; Hong, M. H. Wettability Transition of Laser Textured Brass Surfaces Inside Different Mediums. *Appl. Surf. Sci.* **2018**, *427*, 369−375.
(32) Yong, J.; Chen, F.; Yang, Q.; Jiang, Z.; Hou, X. A review of femtosecond-laser-induced underwater superoleophobic surfaces. *Adv. Mater. Interfaces* **2018**, *5*, No. 1701370.
(33) Bhushan, B.; Jung, Y. C.; Koch, K. Self-cleaning efficiency of artificial superhydrophobic surfaces. *Langmuir* **2009**, *25*, 3240−3248.
(34) Liu, Y.; Li, S.; Niu, S.; Cao, X.; Han, Z.; Ren, L. Bio-inspired micro-nano structured surface with structural color and anisotropic wettability on cu substrate. *Appl. Surf. Sci.* **2016**, *379*, 230−237.
(35) Lee, S. G.; Lim, H. S.; Lee, D. Y.; Kwak, D.; Cho, K. Tunable anisotropic wettability of rice leaf-like wavy surfaces. *Adv. Funct. Mater.* **2013**, *23*, 547−553.
(36) Xia, F.; Jiang, L. Bio-Inspired, Smart, Multiscale Interfacial Materials. *Adv. Mater.* **2008**, *20*, 2842.
(37) Wu, L. Y.; Jiao, Z. B.; Song, Y. Q.; Liu, C. H.; Wang, H.; Yan, Y. Y. Experimental investigations on drag-reduction characteristics of bionic surface with water-trapping microstructures of fish scales. *Sci. Rep.* **2018**, *8*, No. 12186.
(38) Srinivasan, S.; Kleingartner, J. A.; Gilbert, J. B.; Cohen, R. E.; Milne, A. J. B.; Mckinley, G. H. Sustainable drag reduction in turbulent Taylor-Couette flows by depositing sprayable superhydrophobic surfaces. *Phys. Rev. Lett.* **2015**, *114*, No. 014501.
(39) Du, P.; Wen, J.; Zhang, Z. Z.; Song, D.; Ouahsine, A.; Hu, H. B. Maintenance of air layer and drag reduction on superhydrophobic surface. *Ocean Eng.* **2017**, *130*, 328−335.
(40) Patankar, N. A. Vapor Stabilizing Substrates for Superhydrophobicity and Superslip. *Langmuir* **2010**, *26*, 8783−8786.
(41) Hu, H. B.; Wang, D. Z.; Bao, L. Y.; Wen, J.; Zhang, Z. Z. Maintaining large-scale gas layer by creating wettability difference on surfaces under water. *Acta Phys. Sin.* **2016**, *65*, No. 134701.
(42) Mohanarangam, K.; Cheung, S. C. P.; Tu, J. Y.; Chen, L. Numerical simulation of micro-bubble drag reduction using population balance model. *Ocean Eng.* **2009**, *36*, 863−872.
(43) Hu, H.; Wen, J.; Bao, L.; Jia, L.; Zhou, F.; et al. Significant and stable drag reduction with air rings confined by alternated superhydrophobic and hydrophilic strips. *Sci. Adv.* **2017**, *3*, No. e1603288.

https://doi.org/10.1021/acsomega.1c05507
ACS Omega 2022, 7, 2049−2063